Available online at www.sciencedirect.com

SCIENCE DIRECT®

Journal of Magnetic Resonance 171 (2004) 107–117

JMR
Journal of
Magnetic Resonance

www.elsevier.com/locate/jmr

# Short-time restricted diffusion in a static gradient and the attenuation of individual coherence pathways

Lukasz J. Zielinski*, Martin D. Hürlimann

*Schlumberger-Doll Research, 36 Old Quarry Road, Ridgefield, CT 06877-4108, USA*

Received 14 June 2004; revised 7 August 2004
Available online 11 September 2004

## Abstract

We experimentally explore some of the implications of a recent theoretical study [J. Magn. Reson. 64 (2003) 145] for the measurement of restricted diffusion in connected porous media in a static gradient. In particular, we examine how restriction affects the short-time attenuation of different coherence pathways, all excited with the same sequence of slice-selective radiofrequency (RF) pulses, and how the various pathways make the transition to the long-time or tortuosity regime. We confirm that every pathway contains equivalent diffusional information and, for short times, yields the surface-to-volume ratio ($S/V$) of the confining space. We find also, in agreement with the theoretical predictions, that different pathways are controlled by different time scales and, thus, exhibit different sensitivity to restriction. This property might be exploited when designing optimal sequences to study restricted motion.

*Keywords:* Restricted diffusion; Inhomogeneous fields; Coherence pathways; Stray-field NMR; Off-resonance; CPMG

## 1. Introduction

The problem of using fluid diffusion as a probe of restricted geometries becomes much more complex in systems with strongly inhomogeneous static magnetic fields, such as those present in ex situ NMR, including stray-field imaging (STRAFI) [1], NMR-MOUSE [2], and bore-hole logging applications [3]. In such systems the radiofrequency (RF) pulses are slice selective and, thus, any pulse sequence will necessarily excite a multiplicity of coherence pathways, each with different diffusional attenuation properties. To properly assess the effects of confinement on the total signal, one must understand its effects on individual coherence pathways. In systems with a uniform background field, the most common way to measure restricted diffusion involves encoding the initial and final locations of the spins with short gradient pulses via the pulsed field gradient (PFG) technique [4]. In the limit of narrow gradient pulses, the PFG yields the spins' conditional displacement probability, which contains structural information about the medium. But in systems with permanent static gradients, applying pulsed gradients is not necessary to encode the spins' location and to track their displacements. Given that every one of the excited coherence pathway contains the same structural information, it is not clear a priori whether the PFG technique, with its inherent restrictions due to the narrow-pulse condition [5] and the extra hardware requirements for pulsing the field gradient, should be the preferred technique for probing confined geometries.

The issue of extracting structural information from arbitrary coherence pathways was addressed theoretically in a series of papers [5–8] that developed a general framework for treating restricted diffusion in strongly inhomogeneous fields in the presence of off-resonance RF pulses. Here we experimentally explore some aspects

---

* Corresponding author. Fax: +1 203 438 3819.
*E-mail address:* lzielinski@slb.com (L.J. Zielinski).

1090-7807/$ - see front matter © 2004 Elsevier Inc. All rights reserved.
doi:10.1016/j.jmr.2004.08.006

of the theory pertaining to the short-time regime and the transition to the long-time or *tortuosity* limit. In the short-time limit, the correction due to restriction to the decay of an arbitrary pathway is proportional to the surface-to-volume ratio ($S/V$) of the ambient space and can be computed analytically. The well-known short-time expression for the time-dependent diffusion constant [9]

$$D(t) = D_0\left[1 - \frac{4}{9\sqrt{\pi}}\frac{\sqrt{D_0 t}S}{V}\right], \tag{1}$$

is a special case to which our more-general formulation reduces for the narrow-pulse PFG. In general, one can always define some apparent diffusion constant; but the coefficient multiplying the $S/V$ term will depend both on the particular sequence of RF pulses and on the profile of the applied gradients. In the tortuosity regime, reached after the spins have diffused across the macroscopic heterogeneity length scale of a connected porous medium, the attenuation of each pathway will follow the free-diffusion formula but with a reduced diffusion coefficient

$$D_\infty = \frac{D_0}{F\phi}, \tag{2}$$

where $\phi$ is the porosity of the medium and $F = \sigma_b/\sigma$ its formation factor. Here $\sigma_b$ is the bulk conductivity of the fluid and $\sigma$ the measured conductivity of the fluid-saturated medium, assuming no conduction through the matrix or along the interface [10].

To systematically test the theory, we investigated in detail the first four echoes of the Carr–Purcell–Meiboom–Gill (CPMG) sequence [11,12] in a static gradient, measured in water-filled sintered-glass samples with a range of pore sizes spanning 4 μm to over 200 μm. In general, the signal at every echo will have contributions from many different coherence pathways, each relaxing differently as the echo spacing is varied. We selected out individual pathways with phase cycling rather than trying to separate them in time domain as done, for instance, in the CPMG simulations of Bãlibanu et al. [13] or in bulk-water "one-shot" diffusion measurements of Song and Tang [14]. Our approach allows elimination of any interference between different pathways while acquiring their entire associated echo shapes as well as comparison of diffusional attenuation of different pathways at the same time, which is important when studying transitions between the short-time and long-time regimes.

We examined both the excitation spectra of all the pathways and their diffusion attenuation properties. We found that, just as they exhibit different overall sensitivity to diffusion, different pathways differ in their sensitivity to restriction. We also demonstrated a related phenomenon that the effects of restriction on different pathways are controlled by different time scales. This phenomenon manifests itself, for example, in that, although refocusing at the same time, one pathway may be still in the short-time regime with respect to the geometric structure of the sample, while another may have already reached the tortuosity regime.

## 2. Theoretical development

We follow the notations and the basic framework laid out in [7]. We consider a system of spins diffusing in a homogeneous porous medium, polarized in the $z$-direction by a static uniform-gradient field $B(\mathbf{x}) = B_0 + \mathbf{g}\cdot\mathbf{x}$. The RF field, assumed to be uniform in space, is given by $-2B_1\cos(\omega_0 t + \varphi)\hat{\mathbf{x}}$, where $\varphi$ is the phase of the pulse and $\omega_0 = -\gamma B_0$. We further let $\omega$ be the offset of the local Larmor frequency $\omega \equiv -\gamma\mathbf{g}\cdot\mathbf{x}$, and let $\omega_1 \equiv -\gamma B_1$ measure the amplitude of the RF field. We then make the usual definitions:

$$\begin{aligned} m_+ &\equiv m_x + \mathrm{i}m_y,\\ m_- &\equiv m_x - \mathrm{i}m_y,\\ m_0 &\equiv m_z, \end{aligned} \tag{3}$$

where $m_x$, $m_y$, and $m_z$ are the $x$, $y$, and $z$ components of the magnetization. A general RF pulse acts as a rotation mixing all the magnetization components, $m_q = \sum_{q'}\Lambda_{q,q'}m_{q'}$, with $q, q' = -1, 0, +1$. Here $\Lambda_{q,q'}$ denote the rotation matrix elements that determine the fraction of the magnetization transferred from the $q'$ to the $q$ component. Explicit expressions for the $\Lambda_{q,q'}$ for the case of square RF pulses are given in [15]. Under off-resonance conditions, i.e., when $\omega_1$ cannot be assumed infinite, the $\Lambda_{q,q'}$ will depend on $\omega/\omega_1$ and thus on spatial location. As discussed in [6,7,15], the evolution of the magnetization in an arbitrary pulse train can be naturally analyzed in terms of coherence pathways $\mathbf{q} = \{q_0, q_1, q_2, \ldots, q_n\}$, where each $q_k$ labels the particular magnetization component after the $k$th pulse, with $q_0 = 0$ and $q_n = +1$.[1]

Here we specialize to a particular sequence of RF pulses, with a 90° pulse followed after time $\tau$ by four 180° pulses separated by $2\tau$, as in the beginning of the CPMG sequence. Unlike in the standard CPMG, however, in our experiments we systematically vary the phase of each 180° in increments of $\pi/2$, collecting each of the 256 ($=4^4$) scans independently, while keeping track of the acquisition phase of each echo. Adding and subtracting the $x$ and $y$ channels from all the scans appropriately, using the phase dependence of the various pulse-rotation matrix elements, allows us to select out any desired pathway (including the non-refocusing ones).

---

[1] It has been pointed out to us that the dominant convention is to use $q = -1$ to label the refocusing component [16]; however, for consistency with the work in [6] and [7], we continue using $q_n = +1$ for the refocusing coherence.

In the presence of off-resonance conditions, in order to optimize the signal-to-noise characteristics [17], it is preferable to reduce the spacing between the initial 90° pulse and the first 180° pulse by $t_1 = \omega_1^{-1}$. In our experiments $t_1 \ll \tau$, and hence the extra spacing can be ignored for the purposes of computing diffusional attenuation. If the 90° pulse is applied at time $t = t_1$, the $n$th echo will still refocus at $t = 2n\tau$, and the main effect of the adjustment relevant here will be the extra factor of $\exp(-\mathrm{i}q_1\omega/\omega_1)$ in Eq. (4) below.

The contribution of the pathway $\mathbf{q}$ to the signal measured at time $t$ around the $n$th echo is given by

$$M_{\mathbf{q}}(t) = M_0 R_{\mathbf{q}}(t) A_{\mathbf{q}}(t) \int \mathrm{d}\omega\, \mathscr{G}(\omega) W(\omega) \times \left( \prod_{k=1}^{n} \Lambda_{q_k,q_{k-1}} \right) \mathrm{e}^{-\mathrm{i}q_1\omega/\omega_1} \mathrm{e}^{\mathrm{i}\omega(t-2n\tau)}, \tag{4}$$

where $M_0$ is the total initial magnetization; $\mathscr{G}(\omega)$ gives the density of active spins; $W(\omega)$ is the receiver sensitivity; $R_{\mathbf{q}}(t)$ is the $T_1$ and $T_2$ relaxation; and $A_{\mathbf{q}}(t)$, the relaxation due to diffusion in the gradient. $\mathscr{G}(\omega)$ and $W(\omega)$ for our experiments are plotted in the "First Echo" panel in Fig. 1. The product of the rotation matrix elements with the spin density and the antenna profile

$$\Lambda_{\mathbf{q}}(\omega) \equiv \mathscr{G}(\omega) W(\omega) \left( \prod_{k=1}^{n} \Lambda_{q_k,q_{k-1}} \right) \mathrm{e}^{-\mathrm{i}q_1\omega/\omega_1}, \tag{5}$$

will be referred to as the *spectrum* of the pathway $\mathbf{q}$. Note that it is independent of the echo spacing $2\tau$.

In writing down the expression for the short-time diffusional attenuation of an arbitrary pathway in the CPMG, we again follow the notations of [7]. We let $L_D = \sqrt{D_0\tau}$ be the diffusion length during half the echo spacing and $L_G = (D_0/\gamma g)^{1/3}$ be the *dephasing length*, i.e., the distance the spins diffuse in the gradient $g$ before they acquire the phase of 2π. With these definitions, $(L_D/L_G)^6 = \gamma^2\tau^3 g^2 D_0$. We also introduce the *relaxation length*, $L_\rho = D_0/\rho$, where $\rho$ is the surface relaxivity which depends on the strength of the interactions between the fluid nuclear spins and the solid surfaces [18]. $L_\rho$ determines the length scale of spatial inhomogeneity in the spin concentration in the vicinity of walls. In general, as long as the diffusion length during the entire experiment is shorter than $L_G$, $L_\rho$, and any structural length scales in the medium, the short-time regime will hold (see Section 4.3 for more details). Then, for a pathway $\mathbf{q}$ refocusing at the $n$th echo, we can write

$$A_{\mathbf{q}}(2n\tau) = \exp\left\{ -\frac{2n}{3} \left( \frac{L_D}{L_G} \right)^6 \eta_{\mathbf{q}}^0 \left[ 1 - \alpha_{\mathbf{q}} \frac{L_D S}{V} \right] \right\}, \tag{6}$$

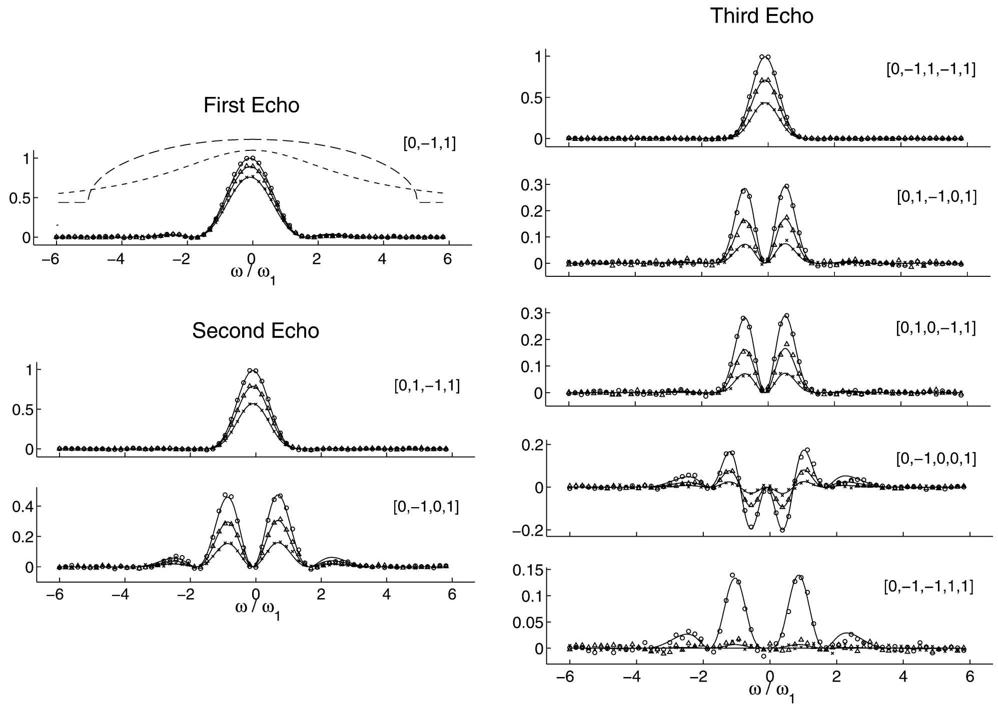

Fig. 1. In-phase component of the measured bulk-water spectrum $M_{\mathbf{q}}(\omega)$ for all the coherence pathways contributing to the first three CPMG echoes. $M_{\mathbf{q}}(\omega)$ is the Fourier transform of the echo shape corresponding to pathway $\mathbf{q}$ and is normalized to $M_0$. The scale of the ordinate axis was adjusted for each panel to show more detail. Circles, triangles, and crosses correspond to the diffusion lengths $L_D$ = 0.64, 2.8, and 3.3 μm, respectively, and the solid lines are the theoretical spectrum, $\Lambda_{\mathbf{q}}(\omega)$ from Eq. (5), weighted with the appropriate $A_q$ and $R_{\mathbf{q}}$ relaxation factors as in Eq. (9). The long-dashed semicircular line in the "First Echo" panel marks the perimeter of the sample, and the short-dashed Lorentzian shape, the sensitivity profile of the receiver coil.

where $\eta^0_{\mathbf{q}}$ gives the bulk attenuation normalized to be 1 for the $n$th direct-echo pathway, and $\alpha_{\mathbf{q}}$ gives the amount of the $S/V$ (surface-to-volume) correction, which is also pathway-dependent. Both $\eta^0_{\mathbf{q}}$ and $\alpha_{\mathbf{q}}$ can be easily computed for any $\mathbf{q}$ using the expressions derived in [6,7]. They are listed for all the pathways contributing to the first three CPMG echoes in Table 1 of [7].

Around the echo at $t = 2n\tau$, the diffusional attenuation of a refocusing pathway can be written as

$$A_{\mathbf{q}}(t) = A_{\mathbf{q}}(2n\tau)\mathrm{e}^{-(1/3)\gamma^2 g^2 (t-2n\tau)^3 D_0} \approx A_{\mathbf{q}}(2n\tau). \tag{7}$$

The approximation in Eq. (7) is valid up to a correction of $\sim 5 \times 10^{-5}$ within the acquisition window in our experiments, which can be kept short due to the short $T_2^*$ fixed by the duration of the 180° pulse.

On the time scales of interest here, since we only consider the early CPMG echoes, the $T_2$ and $T_1$ relaxations for all our samples were well described by single exponentials. In that case, $R_{\mathbf{q}}(t)$ for pathways refocusing around $t = 2n\tau$ can be written as [15]

$$R_{\mathbf{q}}(t) = \exp\left\{-\frac{t-2n\tau}{T_2}\right\} \exp\left\{-\sum_{k=1}^{n}\left(\frac{q_k^2}{T_2} + \frac{1-q_k^2}{T_1}\right)\tau_k\right\}, \tag{8}$$

where $\tau_1 = \tau$ is the first pulse spacing (again, ignoring the $\omega_1^{-1}$ timing shift), $\tau_k = 2\tau$ for $k = 2,\ldots,n-1$, and $\tau_n = \tau$ is the time between the last RF pulse and the echo peak. Again, as for the diffusional attenuation in Eq. (7), within the acquisition period, $R_{\mathbf{q}}(t) \approx R_{\mathbf{q}}(2n\tau)$. We will from now on write $R_{\mathbf{q}}$ for $R_{\mathbf{q}}(2n\tau)$ and $A_{\mathbf{q}}$ for $A_{\mathbf{q}}(2n\tau)$, since the refocusing pathway $\mathbf{q}$ unambiguously determines the echo $n$ to which it contributes. Eq. (4) can then be rewritten as

$$M_{\mathbf{q}}(t) \simeq M_0 R_{\mathbf{q}} A_{\mathbf{q}} \int \mathrm{d}\omega\, \Lambda_{\mathbf{q}}(\omega) \mathrm{e}^{\mathrm{i}\omega(t-2n\tau)} \tag{9}$$

with the echo shape (time dependence) dominated by the pathway spectrum and the phase factor. All the structural information pertaining to the interactions of the diffusing molecules with the walls of the confining space is contained in $A_{\mathbf{q}}$, which is the quantity of interest for comparison with the short-time theory. Having first confirmed good agreement between the theoretical and experimental spectra for all pathways (see Section 4.1 and Fig. 1), we then use the theoretical spectra, $\Lambda_{\mathbf{q}}(\omega)$ computed from Eq. (5), as the optimal filter when extracting the diffusional attenuation $A_{\mathbf{q}}$ from the data. If $M_{\mathbf{q}}(\omega)$ is the Fourier transform of the measured echo shape for the pathway $\mathbf{q}$, then $A_{\mathbf{q}}$ is obtained using

$$A_{\mathbf{q}} = R_{\mathbf{q}}^{-1} \mathcal{N}^{-1} \int \mathrm{d}\omega M_{\mathbf{q}}(\omega) \left[\Lambda_{\mathbf{q}}(\omega)\right]^*, \tag{10}$$

where $\mathcal{N} = \left[\int \mathrm{d}\omega \Lambda_{\mathbf{q}}(\omega) \Lambda^*_{\mathbf{q}}(\omega)\right]^{1/2}$ and the surface relaxation $R_{\mathbf{q}}$ is determined via Eq. (8) from independent measurements of $T_1$ and $T_2$ (see Section 3). According to Eq. (6), for a given pathway $\mathbf{q}$, $A_{\mathbf{q}}$ is a function of the diffusion length $L_{\mathrm{D}}$, or equivalently of the echo spacing $2\tau$, which is the parameter varied experimentally. Thus, from each pathway, parameters such as the bulk diffusion coefficient or the surface-to-volume ratio can be extracted.

As spelled out in [7], in order for the separation of surface and diffusional relaxation and the pathway spectrum effected in Eqs. (4) or (9) to take place, three conditions must be satisfied. First of all, surface relaxation must be weak throughout the entire experiment, i.e., $-\ln R_{\mathbf{q}} \ll 1$. Second, the distance that the spins traverse in the course of the experiment must be short relative to the width of the excited slice, i.e., $B_1/g \gg \sqrt{D_0 t}$, where $D_0$ is the diffusion coefficient of the bulk fluid. Finally, the medium must be macroscopically homogeneous in the sense that the motion of the spins in the direction of the gradient is impeded on average by the same amount in any slice of the medium. All of these conditions are met in our experiments.

## 3. Experimental details

The samples used were cylindrical plugs, with 3.8 cm diameter and 5.1 cm height, of VitraPOR sintered-glass filters made by Robu-glasfilter.[2] The manufacturer's reported "pore sizes," obtained from the sizes of filtrate particles and thus representative more of the throat than pore diameters, ranged from 4 to 250 μm. They were supplemented by a krypton BET measurement of the total surface-to-volume ratio of each sample. Both values are listed in Table 2. We refer to the various samples using the bottom of the range of their corresponding manufacturer-given sizes; thus, we have the 160, 40, 16, 10, and 4 μm samples.

The plugs were saturated with 0.2 Ω-m brine and measured with an Apollo Tecmag spectrometer in the fringe field of a Nalorac 2 T superconducting magnet. The Larmor frequency was 1.764 MHz and the static gradient 13.17 G cm$^{-1}$ (56 kHz cm$^{-1}$) directed perpendicular to the cylinder axis. At this low field, no effects of susceptibility contrasts were detected. The RF field amplitude was 4.91 G (21 kHz), resulting in the duration of a nominal π-pulse of $t_{\mathrm{p}} = 24$ μs, and the quality factor of the receiver was $Q = 13.4$. We used the dwell time of 4 μs and collected 64 points around each CPMG echo. We did not control the sample temperature directly and thus observed some variation in the bulk diffusion coefficient of water between runs, $D_0 = 2.0 \pm 0.05 \times 10^{-5}$ cm$^2$ s$^{-1}$. Unless otherwise noted, the value of $D_0$ used in all the theoretical calculations was $D_0 = 2.0 \times$

---

[2] Manufacturer's information is available on the Internet at http://www.robu.net.

$10^{-5}$ cm$^2$ s$^{-1}$. At this diffusion coefficient, the gradient in our system corresponds to a dephasing length $L_G = (D_0/\gamma g)^{1/3} = 3.85$ µm. Furthermore, for the purposes of calculating the diffusional attenuation, we ignored the finite duration of the RF pulses, i.e., we took $2\tau$ to be the spacing between the centers of adjacent 180°'s. This is an excellent approximation, since we kept $\tau \gg t_p$.

First, to calibrate the bulk and surface relaxation term $R_{\mathbf{q}}$ in Eqs. 4, 9 and 10, we independently measured the $T_1$ and $T_2$ time constants for each of our samples. $T_1$ was obtained with the usual inversion-recovery sequence [15], while $T_2$ with the standard CPMG with a short echo spacing of $2\tau = 410$ µs to minimize diffusional decay. As discussed at length by Goelman and Prammer [19] and Hürlimann and Griffin [20], under the conditions of strongly inhomogeneous fields (i.e., weak RF), the magnetization decays with some effective relaxation time $T_{2\mathrm{eff}}$, which is a mix of $T_2$, $T_1$, and $T_{1\rho}$. However, for the narrow bandwidth obtained in our experiments by integrating the entire echo in time domain, $T_{2\mathrm{eff}}$ should not deviate by more than a couple of percent from the actual $T_2$. We report the measured $T_2$ and $T_1$ values in Table 2. Given the single-exponential nature of both the transverse and longitudinal decay, it is then a simple matter to compute $R_{\mathbf{q}}$ from Eq. (8) for any value of the echo spacing $2\tau$. Using the measured values of the relaxation rates, one can estimate the surface relaxivity $\rho$ and hence the relaxation length $L_\rho$. We found that it was of the order of 100 µm which is much longer than the relevant diffusion lengths. With respect to surface relaxation, then, the short-time regime will always hold.

Diffusional attenuation of each pathway was measured by varying the echo spacing, linearly in $\tau^3$, between $2\tau = 414$ µs and $2\tau = 15.6$ ms. For each value of $\tau$, therefore, we collected 256 scans, four echoes in each, 64 acquisition points per echo. Individual coherence pathways were then extracted as discussed in Section 2. The corresponding experimental spectra $M_{\mathbf{q}}(\omega)$ were obtained by Fourier transforming the echo shapes, and the theoretical spectra were calculated from Eq. (5), using the expressions for $\Lambda_{q_k q_{k+1}}$ from [15]. Diffusional attenuation was then extracted from the data using Eq. (10) and checked against the theoretical formula in Eq. (6).

## 4. Results

### 4.1. Unrestricted diffusion: bulk brine measurements

In Fig. 1, we plot the spectra $M_{\mathbf{q}}(\omega)$ of all the coherence pathways contributing to the first three CPMG echoes, measured in bulk brine, with three different echo spacings corresponding to the diffusion lengths $L_D = \sqrt{D_0\tau} = 0.64$, 2.8, and 3.3 µm. As explained already, experimental data were obtained by Fourier transforming the echo shapes of each pathway, and the solid theory lines were computed from Eqs. (5) and (9) with $D_0 = 2.0 \times 10^{-5}$ cm$^2$ s$^{-1}$. The agreement between theory and experiment is excellent, showing no distortion of the spectrum even for long diffusion times, and validating the approximations that enter Eq. (9). Similar plots for the sintered-glass samples again show no distortion of the spectra, confirming the "homogeneous medium" assumption. The fourth-echo pathways also agree well with the predicted spectra and we use them in the analysis of restricted samples (see Fig. 4). The slight asymmetry in the side-most lobes, for $|\omega/\omega_1| > 2$, is due to imperfect frequency response of our home-built preamplifier.

Visual examination of the figure already reveals the well-known fact that different pathways decay at different rates. Thus, of the two pathways contributing to the second echo, the direct path $\mathbf{q} = [0, 1, -1, 1]$ decays slower with increasing echo spacing than the stimulated path. Similarly, among the third-echo pathways, the direct pathway again decays the least. This is due to the fact that, for the direct pathway, each 180° restarts the clock by completely refocusing the excited spins; the other paths, on the other hand, retain the memory of how far the spins have travelled since the initial 90°. In restricted samples discussed later, the same effect will be responsible for fixing the relevant diffusion length for the direct path at $\sqrt{\sim D_0\tau}$ even for higher echoes.

The fastest decaying pathway in the third echo is $\mathbf{q} = [0, -1, -1, 1, 1]$ which is none other than the familiar Hahn echo (i.e., first CPMG echo) but corresponding to the echo spacing of $4\tau$ rather than $2\tau$. This reflects the fact that the Hahn echo maximizes the diffusional attenuation for a given time relative to other pathways, since the spins suffer the greatest dispersion in acquired phase. Note also that even the predicted phase change of the magnetization throughout the sample, evinced by the pathway $\mathbf{q} = [0, -1, 0, 0, 1]$, is well borne out experimentally.

Since we are measuring individual coherence pathways, the diffusional attenuation of the signal is uniform throughout the sample and given by the $A_{\mathbf{q}}$ for a given pathway, as indicated in Eq. (9). Thus, any portion of the spectrum could be used to extract diffusional information, much as in standard one-dimensional imaging. Since our samples are homogeneous, however, as remarked earlier, to optimize the signal-to-noise characteristics, we used the entire spectra filtered with the theoretically computed shape. From any coherence pathway, then, one can extract the diffusion coefficient by fitting along the $\tau^3$ dimension to the corresponding $A_{\mathbf{q}}$ in Eq. (6), letting $S/V \to 0$ as appropriate in bulk fluid. This procedure is valid since the spectrum of any pathway is unaffected by the length of the spacing between the RF pulses; for the early echoes considered

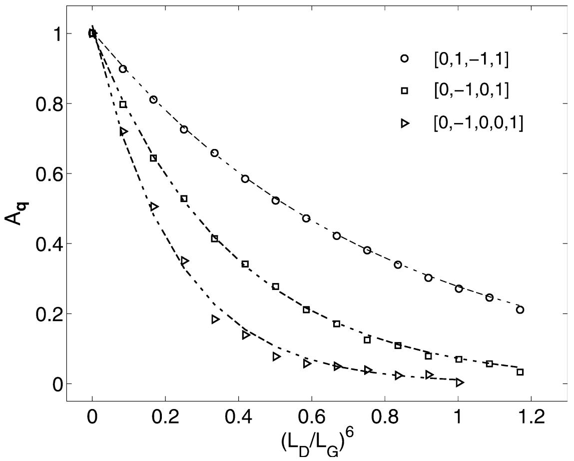

Fig. 2. Measured diffusional attenuation $A_{\mathbf{q}}$ of three different pathways, extracted via Eq. (10) from bulk-water data. Dashed lines are bulk theory (Eq. (6) with $S/V \to 0$) with $D_0 = 2.0 \times 10^{-5}\ \mathrm{cm^2\ s^{-1}}$. As defined in the text $(L_D/L_G)^6 = \gamma^2 g^2 \tau^3 D_0$. Remaining pathways are also well fit with the same $D_0$.

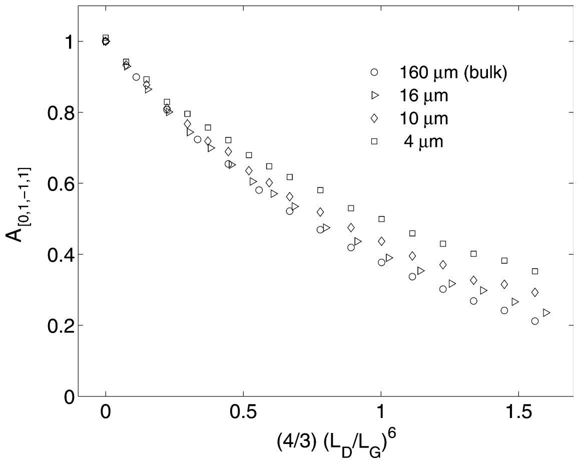

Fig. 3. Measured diffusional attenuation, $A_{\mathbf{q}}$ from Eq. (10), of the second-echo direct pathway, $\mathbf{q} = [0, 1, -1, 1]$, plotted vs. its expected bulk attenuation exponent, for different sintered-glass samples. The more severe the restriction, the smaller the attenuation of the pathway. For these time scales, the 160 μm sample is indistinguishable from bulk fluid.

here, the amount of signal loss due to diffusion out of the excited slice is a fraction of a percent.

We illustrate the results of such fitting for three pathways in Fig. 2; all other pathways were also well fit with the same diffusion coefficient, $D_0 = 2.0 \times 10^{-5}\ \mathrm{cm^2\ s^{-1}}$. For the three pathways shown, the values of $\eta^0_{\mathbf{q}}$ are the well-known expressions for the Hahn and stimulated echoes evaluated at the appropriate echo spacings: $\eta^0_{[0,1,-1,1]} = 1$, $\eta^0_{[0,-1,0,1]} = 2$, and $\eta^0_{[0,-1,0,0,1]} = 7/3$. The data for $\mathbf{q} = [0, -1, 0, 0, 1]$ in Fig. 2 is noisier than for $\mathbf{q} = [0, 1, -1, 1]$ because the corresponding overall amplitude for the former pathway is smaller.

### 4.2. Restricted diffusion: measurement on sintered-glass samples

When the spins encounter restriction to their diffusive motion, they travel less far and sample less of the field inhomogeneity than spins in the bulk. Thus, the more severe the restriction, the smaller the associated diffusional attenuation. This behavior is manifested in Fig. 3, where data for the same pathway, the second-echo direct path $\mathbf{q} = [0, 1, -1, 1]$, are plotted for different Robu samples. On the time scales involved, the 160 μm sample is indistinguishable from bulk water (cf. Fig. 7). The 16 μm sample already deviates from bulk behavior, and the 10 and 4 μm samples deviate progressively more so, in agreement with the simple physical picture.

To examine the effects of restriction quantitatively, we tested the predictions of the short-time theory expounded in Section 2. We examined various coherence pathways for all the samples to check whether they are consistent with the theoretically computed $S/V$ corrections. Fig. 4 shows the results of such analysis for the 16 μm sample. We show there all the pathways contributing to the first four CPMG echoes. Each is plotted vs. its corresponding bulk decay exponent, and so the 'bulk' (dashed) line has the same slope in each panel. The data show that the diffusional attenuation $A_{\mathbf{q}}$ of *all* the pathways is well described by the short-time formula from Eq. (6) (solid lines), with the volume-to-surface ratio $V/S = 6.5 \pm 1$ μm and the bulk diffusion coefficient $D_0 = 2.0 \times 10^{-5}\ \mathrm{cm^2\ s^{-1}}$. Thus, the entire data set can be fit with just one geometrical parameter. The data for longer echo spacings for the last pathway in the third echo and the last five pathways in the fourth echo, were below noise level and are not shown. The overall signal reduction for these pathways is due to the associated geometric factors for this RF sequence ($\Lambda_{\mathbf{q}}$ from Eq. (5)) as well as their intrinsically faster attenuation with increasing echo spacing. The results for the 40 μm sample showed equally good agreement with the theory with $V/S = 9 \pm 1.5$ μm. The 10 and 4 μm samples will be discussed in Section 4.3.

It is clear from the figure that some pathways deviate more from their bulk behavior than others. The direct pathway for each echo is the least affected by restriction, while the fully stimulated paths, i.e., $\mathbf{q} = [0, -1, 0, 1]$, $\mathbf{q} = [0, -1, 0, 0, 1]$, $\mathbf{q} = [0, -1, 0, 0, 0, 1]$, for the second, third, and fourth echoes, respectively, show the greatest amount of deviation. This was to be expected from Eq. (6) since for the two second-echo pathways, for instance, $\alpha_{[0,-1,0,1]} = 0.471$ is over twice as large as $\alpha_{[0,1,-1,1]} = 0.211$ [7]. The $V/S = 6.5 \pm 1$ μm that fits well the 16 μm sample data is 30% higher than the BET value (see Table 2). As discussed in more detail in Section 5, this is not surprising, since gas adsorption is sensitive to structure on sub-micron length scales, smoothed out with a diffusion measurement, resulting in a larger measured BET surface.

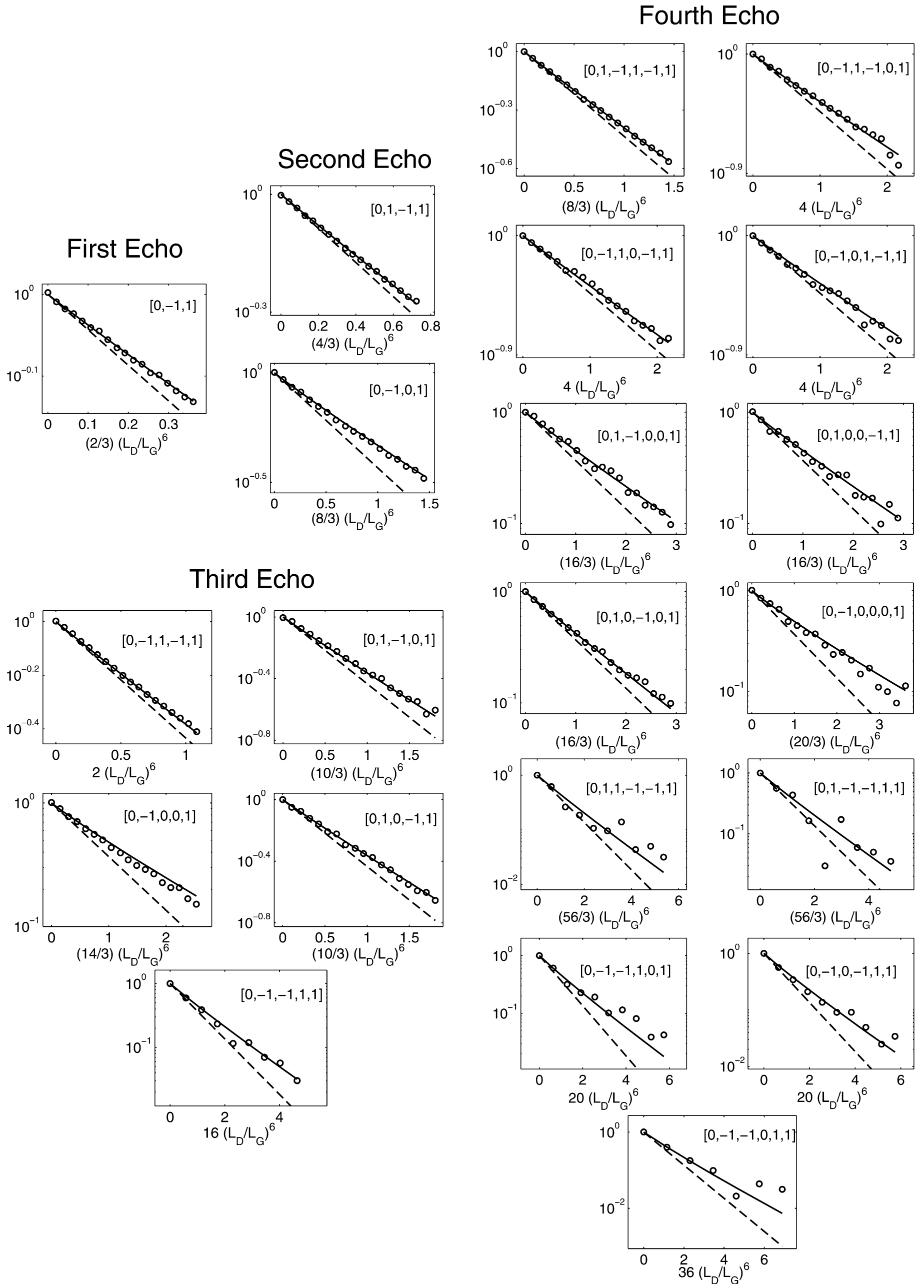

Fig. 4. Measured diffusional attenuation, $A_{\mathbf{q}}$ from Eq. (10), for all the pathways contributing to the first four CPMG echoes, plotted vs. their respective bulk attenuation exponents for the 16 μm sample. Dashed lines indicate the expected bulk decays and, thus, have the same slope in all panels. Solid lines are the theory from Eq. (6) with $V/S = 6.5$ μm and $D_0 = 2.0 \times 10^{-5}\ \mathrm{cm}^2\ \mathrm{s}^{-1}$.

## *4.3. Time scales governing different pathways: validity of the short- and long-time regimes*

Now we explore the interesting phenomenon, theoretically predicted in [6], that the effects of restriction on different coherence pathways are controlled by different time scales. In an ideal PFG experiment, the relevant diffusion time is given by the spacing between the narrow gradient pulses, with the resolution fixed by the pulse duration. When the gradient is static, the only available ruler length is given by the spacing between the RF pulses. For the Hahn echo, $\mathbf{q} = [0,-1,1]$, forming at $t = 2\tau$, for example, the relevant diffusion time is set by $t_{\mathbf{q}} \sim 2\tau$. In multi-pulse sequences, which RF pulse spacing sets the relevant time scale $t_{\mathbf{q}}$ will depend on the particular coherence pathway $\mathbf{q}$. Specializing again to the CPMG with the 180°'s separated by $2\tau$, for the stimulated pathway $\mathbf{q} = [0,-1,0,1]$, for example, we will have $t_{\mathbf{q}} \sim 4\tau$, while for $\mathbf{q} = [0,-1,0,0,1]$, $\tau_{\mathbf{q}} \sim 6\tau$. For the direct CPMG pathway, by contrast, the relevant time scale is set by the spacing between two *adjacent* 180° pulses, regardless of the duration of the entire pulse train [6,21]. This comes about because, for this pathway, the clock is effectively reset at each 180° pulse. Thus, both for $\mathbf{q} = [0, 1, -1, 1]$ and $\mathbf{q} = [0, -1, 1, -1, 1]$, the direct pathways corresponding to the two stimulated pathways mentioned above, the relevant time unit $t_{\mathbf{q}} \sim 2\tau$, same as for the Hahn echo.

The short-time regime for a pathway $\mathbf{q}$ obtains when the diffusion length $\sqrt{D_0 t_{\mathbf{q}}}$ is the shortest length scale in the system, i.e., is shorter than the relaxation length $L_\rho$, the dephasing length $L_G$, and any structural sizes of the medium, set, in our case, by $V/S$. The long-time or tortuosity regime is reached when the diffusion length $\sqrt{D_0 t_{\mathbf{q}}}$ is of the order of the macroscopic length scale of the medium and the attenuation follows free-diffusion formulas with a reduced diffusion coefficient $D_\infty$. As we increase the pulse spacing $2\tau$, therefore, the direct pathway should remain in the short-time regime longer than the stimulated pathways and be the last one to make the transition to the tortuosity regime.

We illustrate this behavior on the 10 and the 4 μm samples. In both, we find that the direct pathway for all the echoes is well fit with the volume-to-surface ratio $V/S = 4.5 \pm 1$ μm for the 10 μm sample and $V/S = 2.5 \pm 0.5$ μm for the 4 μm sample. Other pathways, however, show significant deviation from the short-time behavior and cannot be consistently fit with a single $V/S$. In fact, they seem to lie already in the tortuosity regime, with $D_\infty$ given by the simple bead-pack formula [10,22], $D_\infty/D_0 = \sqrt{\phi}$, where $\phi$ is the porosity of the sample. Then $D_\infty/D_0 = 0.64$ for the 10 μm sample and $D_\infty/D_0 = 0.57$ for the 4 μm sample, as we confirmed with an independent stimulated-echo measurement which allowed us to reach 30 μm diffusion lengths.

In Figs. 5 and 6, we plot two sets of pathways, $\mathbf{q} = [0, 1, -1, 1]$ and $\mathbf{q} = [0, -1, 0, 1]$, contributing to the second echo; and $\mathbf{q} = [0, -1, 1, -1, 1]$ and $\mathbf{q} = [0, -1, 0, 0, 1]$, contributing to the third echo. In both figures, the direct paths in each panel remain well described by the short-time theory (solid line) throughout the entire domain. For the 10 μm sample, the stimulated path in Fig. 5A diverges from the short-time theory line after $(L_D/L_G)^6 \sim 0.2$ and soon makes a transition to the tortuosity limit (dashed line). In Fig. 5B, the stimulated path does not appear to follow the short-time theory at all; rather, it is described by the tortuosity limit from the start. For the 4 μm sample, as expected due to smaller pore sizes, the divergence of the stimulated paths from the short-time theory is even more dramatic. Here, both $\mathbf{q} = [0, -1, 0, 1]$ in Fig. 6A and $\mathbf{q} = [0, -1, 0, 0, 1]$ in Fig. 6B follow the tortuosity line from the very beginning.

It is not possible to analytically compute the thresholds for the onset of the short-time and long-time limits in arbitrary complex geometries. However, we were able to quantitatively account for the behavior of the pathways in Figs. 5 and 6 by referring to the data available in the literature on the narrow-pulse PFG and extrapolating to the case of arbitrary pathways in a static gradient considered in the present work. We start by defining the relevant diffusion length $L_{\mathbf{q}}$ for the pathway $\mathbf{q}$ via

$$L_{\mathbf{q}} = \left(9\sqrt{\pi}/4\right)\alpha_{\mathbf{q}} L_D, \tag{11}$$

whereby Eq. (6) becomes

$$A_{\mathbf{q}} = \exp\left\{-\frac{2n}{3}\left(\frac{L_D}{L_G}\right)^6 \eta^0_{\mathbf{q}}\left[1 - \frac{4}{9\sqrt{\pi}}\frac{L_{\mathbf{q}} S}{V}\right]\right\}, \tag{12}$$

similar in form to the expression for the time-dependent diffusion coefficient in Eq. (1). If $D(t)$ is measured with a PFG experiment with narrow gradient pulses spaced by $t = 2n\tau$, then the corresponding $L_{\mathbf{q}}$ will be $L_{\mathrm{NPA}} = \sqrt{D_0 2n\tau} = \sqrt{2n}L_D$, where NPA stands for *narrow-pulse approximation*.

Numerical simulations of [9] and [10] and the experimental studies in bead packs [23,24] and sand grains

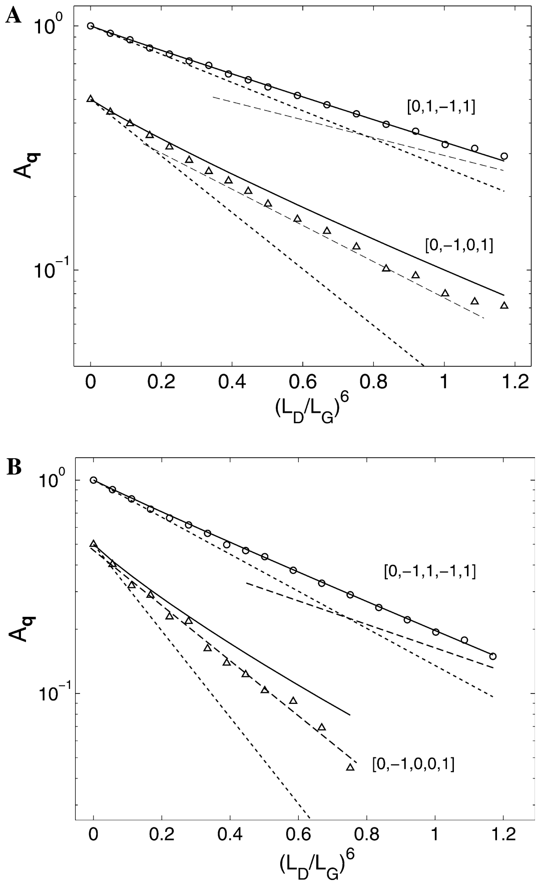

Fig. 5. Different pathways are controlled by different time scales: 10 μm sample. The direct pathway, circles, and the stimulated pathway (offset for clarity), triangles, for the second (A) and third (B) echoes. Solid lines mark the short-time theory for each pathway, Eq. (6) with $V/S = 4.5$ μm, the dotted lines mark their respective bulk decays, and the dashed lines, the slopes of the tortuosity limits with $D_\infty/D_0 = \sqrt{\phi} = 0.64$. Although contributing to the same echo, the direct path in each panel remains in the short-time limit, while the stimulated path already makes the transition to the long-time or tortuosity regime.

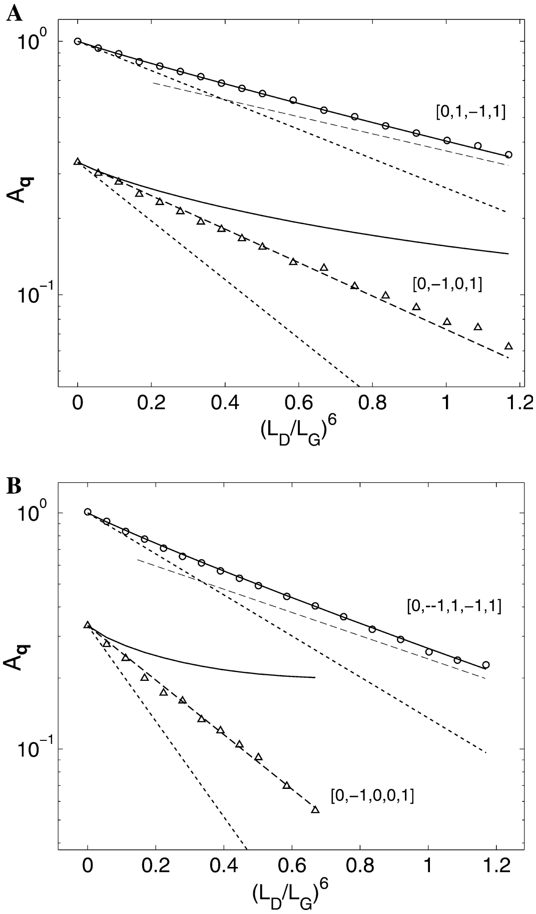

Fig. 6. Different pathways are controlled by different time scales: 4 μm sample. Here the non-direct pathways leave the short-time regime sooner than for the 10 μm sample and thus deviate more strongly from the short-time theory (solid lines, Eq. (6) with $V/S = 2.5$ μm) than in Fig. 5. The tortuosity (dashed) lines are drawn with $D_\infty/D_0 = \sqrt{\phi} = 0.57$.

[25], show that, for the narrow-pulse PFG, the short-time behavior begins to break down for $L_{\mathrm{NPA}} \sim \beta V/S$, where $\beta$ can range from 1 to 1.5, depending both on the sample and on the precise cut-off criteria. We found that $\beta = 1.2$ worked best for our experiments. We then make the ansatz that, for *any* pathway **q**, the threshold length for the onset of the short time regime also be given by $L_{\mathbf{q}} \sim \beta V/S$. This is equivalent to claiming that, for any pathway, the short-time regime breaks down when the the associated $S/V$ correction term in Eq. (6) or Eq. (12) becomes $\sim \beta 4/9\sqrt{\pi} \sim 0.3$. This is a sensible requirement since the structure of the higher-order corrections, following the cumulant expansion, is the same for all the pathways, so that these corrections remain in a similar relation to the $S/V$ term for all pathways. One would expect, therefore, that for any pathway they become significant when the $S/V$ term reaches some fixed threshold value. Having made the ansatz, one can use Eq. (11) and the $\alpha_{\mathbf{q}}$ coefficients listed in [7] to compute the transitional or critical $L_{\mathrm{D}}$ corresponding to each pathway via

$$L_{\mathrm{D}}^{\mathrm{c}} = \left(4/9\sqrt{\pi}\right)\alpha_{\mathbf{q}}^{-1}(\beta V/S). \tag{13}$$

The $L_{\mathbf{q}}$ and $L_{\mathrm{D}}^{\mathrm{c}}$ for the four pathways under consideration are given in Table 1. Note that $L_{\mathbf{q}}$ for the stimulated pathways, which effectively spread the gradient encoding and decoding periods over $\tau$, is a little shorter than the corresponding narrow-pulse PFG length, $L_{\mathrm{NPA}}$, which assumes all the encoding and decoding takes place instantaneously. The $L_{\mathbf{q}}$ for the direct pathways, on the other hand, is much shorter than the corresponding $L_{\mathrm{NPA}}$, due to the refocusing of magnetization at each 180°. Conversely, for a given surface-to-volume ratio, the critical lengths $L_{\mathrm{D}}^{\mathrm{c}}$ for the direct pathways are considerably longer than those for the stimulated pathways, reflecting the fact that the direct path remains in the short-time regime for longer echo spacings.

Since media with monodispersed pore sizes, such as our samples, are characterized by only one structural length scale, the onset of the tortuosity regime will also be governed by $V/S$. Consistent with the bead-pack data cited above, we found that the transition occurs near $L_{\mathrm{D}} \sim 1.1 L_{\mathrm{D}}^{\mathrm{c}}$, where $L_{\mathrm{D}}^{\mathrm{c}}$, Eq. (13), marks the short-time regime. We put all this information together in Fig. 7, where we map out the different regimes for the four pathways from Figs. 5 and 6. The solid lines are given by $L_{\mathrm{D}} = L_{\mathrm{D}}^{\mathrm{c}}$, dashed lines by $L_{\mathrm{D}} = 1.1 L_{D}^{\mathrm{c}}$, and the dotted lines, marking off the region where the $S/V$ correction is less than 5%, are given by $L_{\mathrm{D}} = 0.2 L_{\mathrm{D}}^{\mathrm{c}}$. We emphasize that Fig. 7 is not just a sketch but a quantitative phase diagram. The five samples used in our experiments are marked by triangles along the $V/S$ axis (normalized by the dephasing length $L_{\mathrm{G}} = 3.85$ μm) according to their measured NMR volume-to-surface ratio (see Table 2). For each sample, our measurement scheme, i.e., varying the CPMG pulse spacing, corresponds to moving along the vertical direction in the phase diagram.

The results on all the samples can be understood with the help of Fig. 7. In the 160 μm sample, the $S/V$ correction is too small to be detected, and hence all the pathways are effectively in the free-diffusion regime. The 40 and 16 μm samples both fall within the short-time regime, and thus all pathways are well described by the short-time theory (see Fig. 4). For the 4 and 10 μm

Table 1
The length scale $L_{\mathbf{q}}$ probed by the pathway **q**, Eq. (11), and the threshold or critical diffusion length $L_{\mathrm{D}}^{\mathrm{c}}$ that marks the onset of the short-time regime, Eq. (13) with $\beta = 1.2$, for the four pathways considered in Figs. 5–7

| Pathway **q** | $L_{\mathbf{q}}/L_{\mathrm{D}}$ | $L_{\mathbf{q}}/L_{\mathrm{NPA}}$ | $L_{\mathrm{D}}^{\mathrm{c}} S/V$ |
|---|---|---|---|
| $[0, 1, -1, 1]$ | 0.84 | 0.42 | 1.4 |
| $[0, -1, 0, 1]$ | 1.88 | 0.94 | 0.64 |
| $[0, -1, 1, -1, 1]$ | 0.89 | 0.36 | 1.3 |
| $[0, -1, 0, 0, 1]$ | 2.35 | 0.96 | 0.52 |

$L_{\mathrm{D}} = \sqrt{D_0 \tau}$ is the diffusion length during half the echo spacing and $L_{\mathrm{NPA}} = \sqrt{2n} L_{\mathrm{D}}$ is the corresponding $L_{\mathbf{q}}$ for the narrow-pulse PFG experiment with pulsed gradients spaced by $2n\tau$.

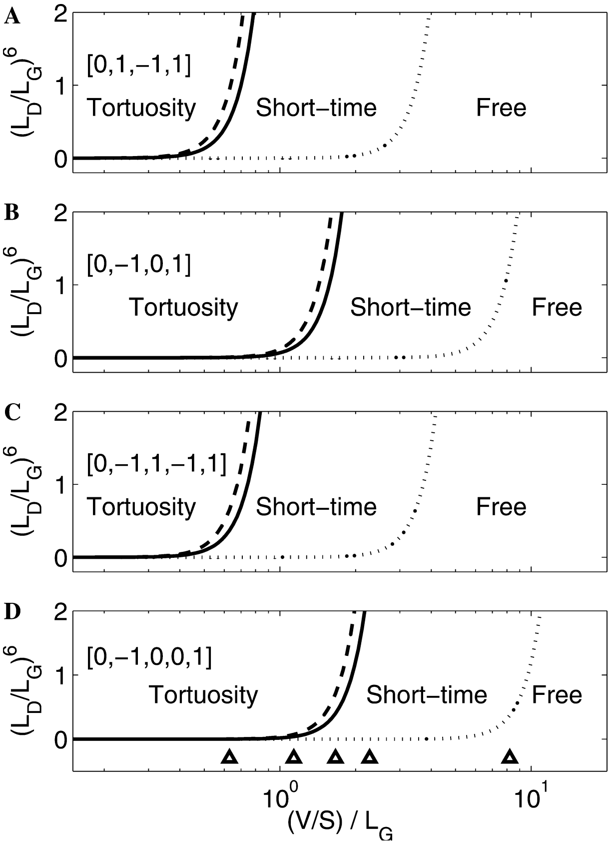

Fig. 7. Three diffusion regimes relevant in connected porous media, free-diffusion, short-time, and tortuosity, for the direct and stimulated pathways contributing to the second echo, (A and B), and to the third echo (C and D). Solid lines give $L_D = L_D^c$ for each pathway (see Table 1), dashed lines give the tortuosity threshold, $L_D = 1.1L_D^c$, and the dotted lines mark the contours where the restriction (*S*/*V*) correction is ~5%. The triangles along the abscissa indicate the position of our sintered-glass samples according to their NMR *V*/*S* (see Table 1). Varying the pulse spacing $2\tau$ has the effect of traversing the phase space along vertical lines.

samples, only the direct pathways are within the short-time regime, while the third-echo stimulated path, $\mathbf{q} = [0, -1, 0, 0, 1]$, lies entirely within the tortuosity limit for both. Finally, as shown in Fig. 5A, the second-echo stimulated path, $\mathbf{q} = [0, -1, 0, 1]$, for the 10 μm sample, starts in the short-time regime and makes a transition to the tortuosity regime as the pulse spacing is increased. Since the abscissa is scaled in units of the dephasing length $L_G$, one can move along it either by considering samples with different pore sizes, as we have done, or by varying the strength of the gradient for a given sample. Thus, by following a diagram like the one in Fig. 7, one can place the sample within the desired regime by exploiting the interplay between $L_G$ and $L_D$.

## 5. Measuring the surface with diffusion: general remarks

The theory of short-time diffusion as a probe of the confining surface, both for the usual $D(t)$ and for the more general case exploited in this paper, hinges on the assumption of a locally smooth surface, i.e., flat with respect to the relevant diffusion length. In any physical system, no surface is perfectly smooth, certainly not if probed down to atomic dimensions. This does not mean, of course, that the mathematical model used is never applicable. A measurement of the surface area necessarily depends on the length of the "ruler" used. Any surface roughness on length scales much shorter than the ruler will not invalidate the smoothness assumption, but only reestablish the effective surface appropriate to use in the model.

Diffusion tracked by NMR gives one example of a surface measurement, with a ruler length fixed by the appropriate diffusion length. Most porous media, both man-made such as cements or concretes and natural such as rocks and sands, will have at least some surface roughness on length scales shorter than the shortest accessible diffusion lengths. Clearly, the NMR measurement is not sensitive to such small structure. Yet, in a large variety of systems, including fractal-like sand grains examined by [25], one still observes a correction to the bulk diffusion coefficient that is proportional to $\sqrt{D_0 t}$. This strongly suggests that diffusion smooths over such surface roughness, creating an effective "NMR surface" that satisfies the requirements of the theory. This NMR surface, then, can be thought of as the actual surface measured with a ruler of length set by the relevant diffusion length.

In contrast with NMR, gas adsorption (BET) techniques in principle measure the surface down to structure on atomic length scales. One expects, therefore, the surface measured with the BET to be larger than the NMR surface [26], which is what we have found

Table 2
Sample specifications

| Sample | RobuGlas list name | $T_2$ (s) | $T_1$ (s) | Porosity (%) | BET *V*/*S* (μm) | NMR *V*/*S* (μm) | Throat size (μm) |
|---|---|---|---|---|---|---|---|
| "160 μm" | Robu 0 | 2.07 | 2.2 | 30.3 | 13.8 | 35 ± 10 | 160–250 |
| "40 μm" | Robu C | 1.82 | 1.9 | 38.0 | 9.6 | 9.0 ± 1.5 | 40–60 |
| "16 μm" | Robu 3 | 1.34 | 1.9 | 41.5 | 4.6 | 6.5 ± 1 | 16–40 |
| "10 μm" | Robu 4 | 1.09 | 1.4 | 41.5 | 2.7 | 4.5 ± 0.5 | 10–16 |
| "4 μm" | Robu F | 0.43 | 0.64 | 32.5 | 0.9 | 2.5 ± 0.5 | 4–5.5 |

BET was performed with krypton gas adsorption. "Throat size" refers to the number quoted by RobuGlas and derives from filtered particle sizes. "NMR *V*/*S*" was extracted using the short-time theory, Eq. (6), except for the 160 μm sample, for which the usual stimulated echo sequence was used. The sample names used throughout the text, i.e., "40 μm" sample, etc., refer to their corresponding lower cut-off throat sizes.

for our fused glass beads. Furthermore, the smaller the actual pore sizes, the greater the proportion of the surface will derive from structure smaller than the diffusion ruler length, resulting in a greater relative discrepancy between the NMR and BET measurements. The data for the four smaller samples in Table 2 bear out that trend as well. For the 160 μm sample, on the other hand, the BET *V*/*S* does not scale relative to the smaller samples in proportion with the pore throat size given in the last column. This indicates that, except for a few large channels, the structure within the sample is dominated by lengths not substantially larger than in the 40 μm sample. The NMR *V*/*S* for this sample, however, does increase in the right proportion, suggesting that, for the purposes of flow through porous media, it is the NMR surface, rather than the BET surface, that is the more relevant quantity. Another example where the BET surface may be of dubious usefulness is fluid-saturated clays, which can swell considerably relative to their dried state necessary for a BET measurement. Thus, in many physical systems, the concept of a "true" surface area may be simply ill-posed. BET can give one value, NMR another, and the two need not necessarily coincide; which one is more useful will depend on the application at hand.

## 6. Conclusion

We have experimentally validated the recent theory that computes the short-time diffusional attenuation for an arbitrary coherence pathway in a static gradient in the presence of restriction and slice-selective RF pulses. We have found that all pathways contain equivalent diffusional information and, for short times, can be used to extract the surface-to-volume ratio of the confining space. We also confirmed that different pathways show different sensitivity to diffusion and that they are controlled by different time scales. For the direct CPMG pathway, for example, the relevant time scale is set not by the echo-formation time, but rather by the spacing between two adjacent 180° pulses. Thus, it remains in the short-time limit longer than other pathways. A potential application of this phenomenon to the probing of small structure will be investigated elsewhere.

## References

[1] P.J. McDonald, Stray field magnetic resonance imaging, Prog. Nucl. Magn. Reson. Spectrosc. 30 (1997) 69–99.

[2] G. Eidmann, R. Savelsberg, P. Blümer, B. Blümich, The NMR-MOUSE a mobile universal surface explorer, J. Magn. Reson. Ser. A 122 (1996) 104–109.

[3] R.L. Kleinberg, Well logging, in: Encyclopedia of Nuclear Magnetic Resonance, Vol. 8, Wiley, Chichester, 1996, pp. 4960–4969.

[4] E.O. Stejskal, J.E. Tanner, Spin diffusion measurements: spin echoes in the presence of a time-dependent field gradient, J. Chem. Phys. 42 (1965) 288.

[5] L.J. Zielinski, P.N. Sen, Effects of finite-width pulses in the pulsed-field gradient measurement of the diffusion coefficient in connected porous media, J. Magn. Reson. 165 (2003) 153–161.

[6] L.J. Zielinski, P.N. Sen, Combined effects of diffusion, nonuniform-gradient magnetic fields, and restriction on an arbitrary coherence pathway, J. Chem. Phys. 119 (2003) 1093.

[7] L.J. Zielinski, P.N. Sen, Restricted diffusion in grossly inhomogeneous fields, J. Magn. Reson. 164 (2003) 145–153.

[8] L.J. Zielinski, Effect of internal gradients in the nuclear magnetic resonance measurement of the surface-to-volume ratio, J. Chem. Phys. 121 (2004) 352.

[9] P.P. Mitra, P.N. Sen, L.M. Schwartz, Short-time behavior of the diffusion coefficient as a geometrical probe of porous media, Phys. Rev. B 47 (1993) 8565.

[10] P.N. Sen, L.M. Schwartz, P.P. Mitra, B.I. Halperin, Surface relaxation and the long-time diffusion coefficient in porous media: periodic geometries, Phys. Rev. B 49 (1994) 215.

[11] H.Y. Carr, E.M. Purcell, Effects of diffusion on free precession in NMR experiments, Phys. Rev. 94 (1954) 630.

[12] S. Meiboom, D. Gill, Compensation for pulse imperfections in Carr–Purcell NMR experiments, Rev. Sci. Instrum. 29 (1958) 688.

[13] F. Bălibanu, K. Hailu, R. Eymael, D.E. Demco, B. Blümich, Nuclear magnetic resonance in inhomogeneous magnetic fields, J. Magn. Reson. 145 (2000) 246–258.

[14] Y.-Q. Song, X. Tang, A one-shot method for measurement of diffusion, J. Magn. Reson. 170 (2004) 136–148.

[15] M.D. Hürlimann, Diffusion and relaxation effects in general stray field NMR experiments, J. Magn. Reson. 148 (2001) 367–378.

[16] R.R. Ernst, G. Bodenhausen, A. Wokaun, Principles of Nuclear Magnetic Resonance in One and Two Dimensions, Oxford University Press, New York, 1994.

[17] M.D. Hürlimann, Optimization of timing in the Carr–Purcell–Meiboom–Gill sequence, Magn. Reson. Imag. 19 (2001) 375–378.

[18] P.Z. Wong, Methods in the Physics of Porous Media, Academic Press, London, 1999.

[19] G. Goelman, M. Prammer, The CPMG pulse sequence in strong magnetic field gradients with applications to oil-well logging, J. Magn. Reson. Ser. A 113 (1995) 11–18.

[20] M.D. Hürlimann, D.D. Griffin, Spin dynamics of Carr–Purcell–Meiboom–Gill-like sequences in grossly inhomogenous $B_0$ and $B_1$ fields and application to NMR well logging, J. Magn. Reson. 143 (2000) 120–135.

[21] P.N. Sen, A. André, S. Axelrod, Spin echoes of nuclear magnetization diffusing in a constant magnetic field gradient and in a restricted geometry, J. Chem. Phys. 111 (1999) 6548.

[22] P.N. Sen, C. Scala, M.H. Cohen, A self-similar model for sedimentary rocks with application to the dielectric constant of fused glass beads, Geophysics 46 (1981) 781.

[23] L. Latour, P. Mitra, R. Kleinberg, C. Sotak, Time-dependent diffusion coefficient of fluids in porous media as a probe of surface-to-volume ratio, J. Magn. Reson. Ser. A 101 (1993) 342–346.

[24] R.W. Mair, G.P. Wong, D. Hoffman, M.D. Hürlimann, S. Patz, L.M. Schwartz, R.L. Walsworth, Probing porous media with gas diffusion NMR, Phys. Rev. Lett. 83 (1999) 3324.

[25] F. Stallmach, C. Vogt, J. Kärger, K. Helbig, F. Jacobs, Fractal geometry of surface areas of sand grains probed by pulsed field gradient NMR, Phys. Rev. Lett. 88 (2002) 105505.

[26] M.D. Hürlimann, K.G. Helmer, L.L. Latour, C.H. Sotak, Restricted diffusion in sedimentary rocks. Determination of surface-area-to-volume ratio and surface relaxivity, J. Magn. Reson. Ser. A 111 (1994) 169–178.